

Supplementary Material for “Observation of a superradiant phase transition with emergent cat states”

Ri-Hua Zheng,^{1,*} Wen Ning,^{1,*} Ye-Hong Chen,^{1,2,3,*} Jia-Hao Lü,¹ Li-Tuo Shen,¹ Kai Xu,^{4,5} Yu-Ran Zhang,^{6,2,3} Da Xu,⁷ Hekang Li,⁵ Yan Xia,¹ Fan Wu,¹ Zhen-Biao Yang,^{1,†} Adam Miranowicz,^{2,8} Neill Lambert,² Dongning Zheng,^{4,5} Heng Fan,^{4,5} Franco Nori,^{2,3,9,‡} and Shi-Biao Zheng^{1,§}

¹*Fujian Key Laboratory of Quantum Information and Quantum Optics,
College of Physics and Information Engineering,
Fuzhou University, Fuzhou, Fujian 350108, China*

²*Theoretical Quantum Physics Laboratory, RIKEN Cluster for Pioneering Research, Wako-shi, Saitama 351-0198, Japan*

³*Quantum Information Physics Theory Research Team,
RIKEN Center for Quantum Computing (RQC), Wako-shi, Saitama 351-0198, Japan*

⁴*Institute of Physics and Beijing National Laboratory for Condensed Matter Physics,
Chinese Academy of Sciences, Beijing 100190, China*

⁵*CAS Center for Excellence in Topological Quantum Computation,
University of Chinese Academy of Sciences, Beijing 100190, China*

⁶*School of Physics and Optoelectronics, South China University of Technology, Guangzhou 510640, China*

⁷*Department of Physics, Zhejiang University, Hangzhou, Zhejiang 310027*

⁸*Faculty of Physics, Adam Mickiewicz University, 61-614 Poznań, Poland*

⁹*Department of Physics, University of Michigan, Ann Arbor, Michigan 48109-1040, USA*

(Dated: August 11, 2023)

Contents

S1. Effective quantum Rabi model	2
A. Derivation of the effective quantum Rabi Hamiltonian	2
B. Superradiant phase transition under ideal conditions	3
S2. Experimental setup, device parameters, and pulse sequence	4
S3. Control of quenching dynamics	6
A. Time-dependence of the normalized coupling parameter ξ	6
B. Control of the effective qubit frequency Ω	7
C. Control of the effective resonator frequency δ	7
S4. Effects of off-resonant couplings and decoherence	9
S5. Characterization of the qubit-resonator state	11
A. Photon-number distribution	11
B. Diagonal Wigner matrix elements	12
C. Off-diagonal Wigner matrix elements	14
S6. Measure of the qubit-resonator entanglement	15
S7. Characterization of the super-cat state	16
S8. Numerical simulation of the Dicke-model SPT	16
References	19

*These authors contribute equally to this work.

†Electronic address: zbyang@fzu.edu.cn

‡Electronic address: fnori@riken.jp

§Electronic address: t96034@fzu.edu.cn

S1. EFFECTIVE QUANTUM RABI MODEL

A. Derivation of the effective quantum Rabi Hamiltonian

When the drive is tuned to the carrier, the dynamics is described by the Hamiltonian ($\hbar = 1$ hereafter)

$$H = H_0 + H_I, \quad (\text{S1})$$

where

$$\begin{aligned} H_0 &= (\omega_0 + 2\nu_1) a^\dagger a + \frac{1}{2}[\omega_0 + \varepsilon_1 \cos(\nu_1 t)]\sigma_z, \\ H_I &= \delta a^\dagger a + \frac{1}{2}\varepsilon_2 \cos(\nu_2 t)\sigma_z + (\lambda a^\dagger \sigma_- + K e^{i\omega_0 t} \sigma_- + \text{h.c.}). \end{aligned} \quad (\text{S2})$$

Here, $\sigma_z = |e\rangle\langle e| - |g\rangle\langle g|$ and $\sigma_- = |g\rangle\langle e|$ are Pauli operators for the qubit. Performing the transformation

$$U_0 = \exp \left[i \int_0^t H_0 dt \right], \quad (\text{S3})$$

we obtain the system Hamiltonian in the rotating frame

$$H'_I = \delta a^\dagger a + \frac{1}{2}\varepsilon_2 \cos(\nu_2 t)\sigma_z + \left\{ \exp[-i\mu \sin(\nu_1 t)] [\lambda \exp(2i\nu_1 t) a^\dagger + K] \sigma_- + \text{h.c.} \right\}, \quad (\text{S4})$$

where $\mu = \varepsilon_1/\nu_1$. Using the Jacobi-Anger expansion

$$\exp[i\mu \sin(\nu_1 t)] = \sum_{m=-\infty}^{\infty} J_m(\mu) \exp(im\nu_1 t), \quad (\text{S5})$$

with $J_m(\mu)$ being the m th Bessel function of the first kind, we obtain

$$H'_I = \delta a^\dagger a + \frac{1}{2}\varepsilon_2 \cos(\nu_2 t)\sigma_z + \left(\sum_{m=-\infty}^{\infty} J_m(\mu) \left\{ \lambda \exp[-i(m-2)\nu_1 t] a^\dagger + K \exp(-im\nu_1 t) \right\} \sigma_- + \text{h.c.} \right). \quad (\text{S6})$$

ADC	Analog-to-Digital Converter
DAC	Digital-to-Analog Converter
DC	Direct Current
HEMT	High Electron Mobility Transistor
IQ	In-phase and Quadrature
JPA	Josephson Parametric Amplifier
MC	Mixing Chamber
MS	Microwave Source
NP	Normal Phase
RC	Resistance Capacitance
RI	Read-In
RO	Read-Out
SPT	Superradiant Phase Transition
SP	Superradiant Phase

TABLE S1: Abbreviations used in this supplemental material.

Assuming that $\{|\lambda J_2(\mu)|, |K J_0(\mu)|, \delta, \varepsilon_2\} \ll \nu_1$, we can discard the fast-oscillating terms, thus H'_I reduces to

$$\begin{aligned} H'_I &= [J_2(\mu)\lambda a^\dagger \sigma_- + K J_0(\mu)\sigma_- + \text{h.c.}] + \delta a^\dagger a + \frac{1}{2}\varepsilon_2 \cos(\nu_2 t)\sigma_z \\ &= \frac{1}{2}B_0\sigma_x + \frac{1}{2}\varepsilon_2 \cos(\nu_2 t)\sigma_z + \delta a^\dagger a + \eta(X\sigma_x - Y\sigma_y), \end{aligned} \quad (\text{S7})$$

where $B_0 = 2K J_0(\mu)$, $\eta = \lambda J_2(\mu)/2$, $X = a^\dagger + a$, $Y = i(a^\dagger - a)$, $\sigma_x = \sigma_- + \sigma_-^\dagger$, and $\sigma_y = i\sigma_- - i\sigma_-^\dagger$. Under the transformation $\exp(iB_0\sigma_x t/2)$, the system Hamiltonian in the moving frame becomes

$$\begin{aligned} H''_I &= \eta\{X\sigma_x - Y[\cos(B_0 t)\sigma_y - \sin(B_0 t)\sigma_z]\} \\ &\quad + \delta a^\dagger a + \frac{1}{2}\varepsilon_2 \cos(\nu_2 t)[\cos(B_0 t)\sigma_z + \sin(B_0 t)\sigma_y]. \end{aligned} \quad (\text{S8})$$

In the limit of $B_0 \gg \eta, \varepsilon_2/2$ and $\nu_2 = B_0$, the fast-oscillating terms can be neglected, and H''_I reduces to the Rabi Hamiltonian

$$H_R = \frac{1}{2}\Omega\sigma_z + \delta a^\dagger a + \eta\sigma_x(a^\dagger + a), \quad (\text{S9})$$

where $\Omega = \varepsilon_2/2$ is the effective qubit frequency.

Some fast-oscillating terms in Eq. (S6) cannot be ignored, and induce additional Stark shifts to the effective qubit- and cavity-frequencies. Detailed discussions about these Stark shifts are shown in Sec. S4.

B. Superradiant phase transition under ideal conditions

In the limit of $\Omega/\delta \rightarrow \infty$, we can diagonalize the Rabi Hamiltonian H_R using a Schrieffer-Wolff transformation [S1]. After applying a unitary operator

$$U_{\text{SW}} = \exp\left[i\frac{\eta}{\Omega}(a^\dagger + a)\sigma_y\right], \quad (\text{S10})$$

and keeping the terms up to second order in the qubit-resonator coupling strengths, Eq. (S9) becomes

$$H_{\text{np}} = \delta a^\dagger a + \frac{\Omega}{2}\sigma_z + \frac{\delta\xi^2}{4}(a + a^\dagger)^2\sigma_z, \quad (\text{S11})$$

which provides a faithful description of the system ground state in the normal phase (NP) of the model, where $\xi = 2\eta/\sqrt{\Omega\delta}$ is a normalized coupling parameter. Equation (S11) shows that the ground-qubit-state subspace $\{|n\rangle|g\rangle\}$ is decoupled from the excited-qubit-state subspace $\{|n\rangle|e\rangle\}$. Therefore, upon a projection $\langle g|H_{\text{np}}|g\rangle$ for $\xi \leq 1$, one can solve the ground eigenstate and eigenvalue of H_R as

$$|\psi_{\text{np}}\rangle = S(r_{\text{np}})|0\rangle|g\rangle, \quad \mathcal{E}_{\text{np}} = \delta\sqrt{1 - \xi^2}, \quad (\text{S12})$$

where $S(r_{\text{np}}) = \exp[(r_{\text{np}}a^{\dagger 2} - r_{\text{np}}^*a^2)/2]$ is the squeezing operator with a real squeezing parameter $r_{\text{np}} = -\frac{1}{4}\ln(1 - \xi^2)$. Thus, the excitation energy \mathcal{E}_{np} is a positive real number for $\xi < 1$ and vanishes at $\xi = 1$, i.e., in the NP.

For $\xi > 1$, the number of photons occupied in the cavity field becomes proportional to Ω/δ and acquires macroscopic occupations, i.e., in the superradiance phase (SP) [S1]. To capture the physics of the SP, we displace the bosonic mode in the Rabi Hamiltonian H_R . For a displacement parameter $\alpha = \sqrt{[\Omega/(4\xi^2\delta)](\xi^4 - 1)}$, we obtain

$$\begin{aligned} H'_R(\pm\alpha) &= D^\dagger(\pm\alpha)H_R D(\pm\alpha) \\ &= \delta a^\dagger a + \frac{\tilde{\Omega}}{2}\tilde{\sigma}_z^\pm + \tilde{\eta}(a + a^\dagger)\tilde{\sigma}_x^\pm + \delta\alpha^2, \end{aligned} \quad (\text{S13})$$

where $\tilde{\Omega} = \xi^2\Omega$, $\tilde{\eta} = \sqrt{\delta\tilde{\Omega}}/(2\xi)$, and

$$D(\alpha) = \exp(\alpha a^\dagger - \alpha^* a), \quad \tilde{\sigma}_z^\pm = |\uparrow^\pm\rangle\langle\uparrow^\pm| - |\downarrow^\pm\rangle\langle\downarrow^\pm|, \quad \tilde{\sigma}_x^\pm = |\uparrow^\pm\rangle\langle\downarrow^\pm| + |\downarrow^\pm\rangle\langle\uparrow^\pm|. \quad (\text{S14})$$

The states

$$|\uparrow^\pm\rangle = \cos(\theta)|e\rangle \pm \sin(\theta)|g\rangle, \quad |\downarrow^\pm\rangle = \mp \sin(\theta)|e\rangle + \cos(\theta)|g\rangle, \quad (\text{S15})$$

are the eigenstates of the terms $(\frac{\Omega}{2}\sigma_z \pm 2\alpha\eta\sigma_x)$ that construct a new qubit eigenstate subspace, where θ obeys

$$\tan\theta = \sqrt{\frac{\xi^2 - 1}{\xi^2 + 1}}. \quad (\text{S16})$$

Then, employing the same procedure used to derive H_{np} , we obtain

$$H_{\text{sp}} = \delta a^\dagger a + \frac{\delta}{4\xi^4} (a^\dagger + a)^2 \tilde{\sigma}_z^\pm + \frac{\Omega}{4} (\xi^2 + \xi^{-2}) \tilde{\sigma}_x^\pm. \quad (\text{S17})$$

Applying the projection $\langle\downarrow^\pm|H_{\text{sp}}|\downarrow^\pm\rangle$, Eq. (S17) becomes

$$H_{\text{sp}} = \delta a^\dagger a - \frac{\delta}{4\xi^4} (a^\dagger + a)^2 - \frac{\Omega}{4} (\xi^2 + \xi^{-2}), \quad (\text{S18})$$

whose excitation energy is found to be $\mathcal{E}_{\text{sp}} = \delta\sqrt{1 - \xi^{-4}}$. The ground eigenstates of the quantum Rabi Hamiltonian H_R for $\xi > 1$ are

$$|\psi_{\text{sp}}\rangle = D(\pm\alpha)S(r_{\text{sp}})|0\rangle|\downarrow^\pm\rangle, \quad (\text{S19})$$

which are degenerate, where $r_{\text{sp}} = -\frac{1}{4}\ln(1 - \xi^{-4})$.

Therefore, H_{np} and H_{sp} are the exact low-energy effective Hamiltonians for the NP ($\xi < 1$) and SP ($\xi > 1$), respectively.

S2. EXPERIMENTAL SETUP, DEVICE PARAMETERS, AND PULSE SEQUENCE

The whole electronics and wiring for our superconducting circuit control are outlined in Fig. S1 [S2, S3]. The superconducting circuit sample, used in our experiment, possesses a bus resonator and five Xmon qubits. Each qubit has its own read-out resonator for reading out its states. The bus resonator has a fixed bare frequency $\omega_p/2\pi = 5.581$ GHz and a photonic decay time $T_{1,p} = 12.9 \mu\text{s}$. Every qubit has two control lines: an XY-control for flipping its states and a Z-control for modulating its frequency, allowing the qubit to flexibly couple with the bus resonator. This, together with the relatively long lifetime of the resonator photons, guarantees the slow quenching manipulation of the qubit-resonator ground state to induce the appearance of the superradiant phase transition (SPT) accompanied by the sudden birth of a photonic mesoscopic superposition of a considerable size. For clarity, Table S1 lists the abbreviations used in this supplemental material.

The XY-controls on the qubits are implemented through the mixing of the low-frequency signals yielded by the IQ channels of two digital-to-analog converters (DACs) and a microwave source (MS). The carrier frequency of the MS is about 5.5 GHz. The Z-controls on the qubits are implemented by two signals: one is produced by the direct-current (DC) biasing line from a low-frequency DC source; the other comes directly from the Z-control of a DAC. The qubit read-out is realized through mixing the signals of the IQ channels of two DACs and an MS with a frequency ~ 6.69 GHz, which output a read-out pulse with multiple tones targeting all resonators for qubit read-out. The output from the circuit is amplified sequentially by an impedance-transformed Josephson parametric amplifier (JPA), high electron mobility transistor (HEMT), and room temperature amplifiers. Then, it is captured and demodulated by analog-to-digital converters (ADCs). Both DACs and ADCs are supported by a field-programmable gate array which reacts at a nanosecond-level speed. The JPA is pumped by an MS with a frequency ~ 13.5 GHz and modulated by

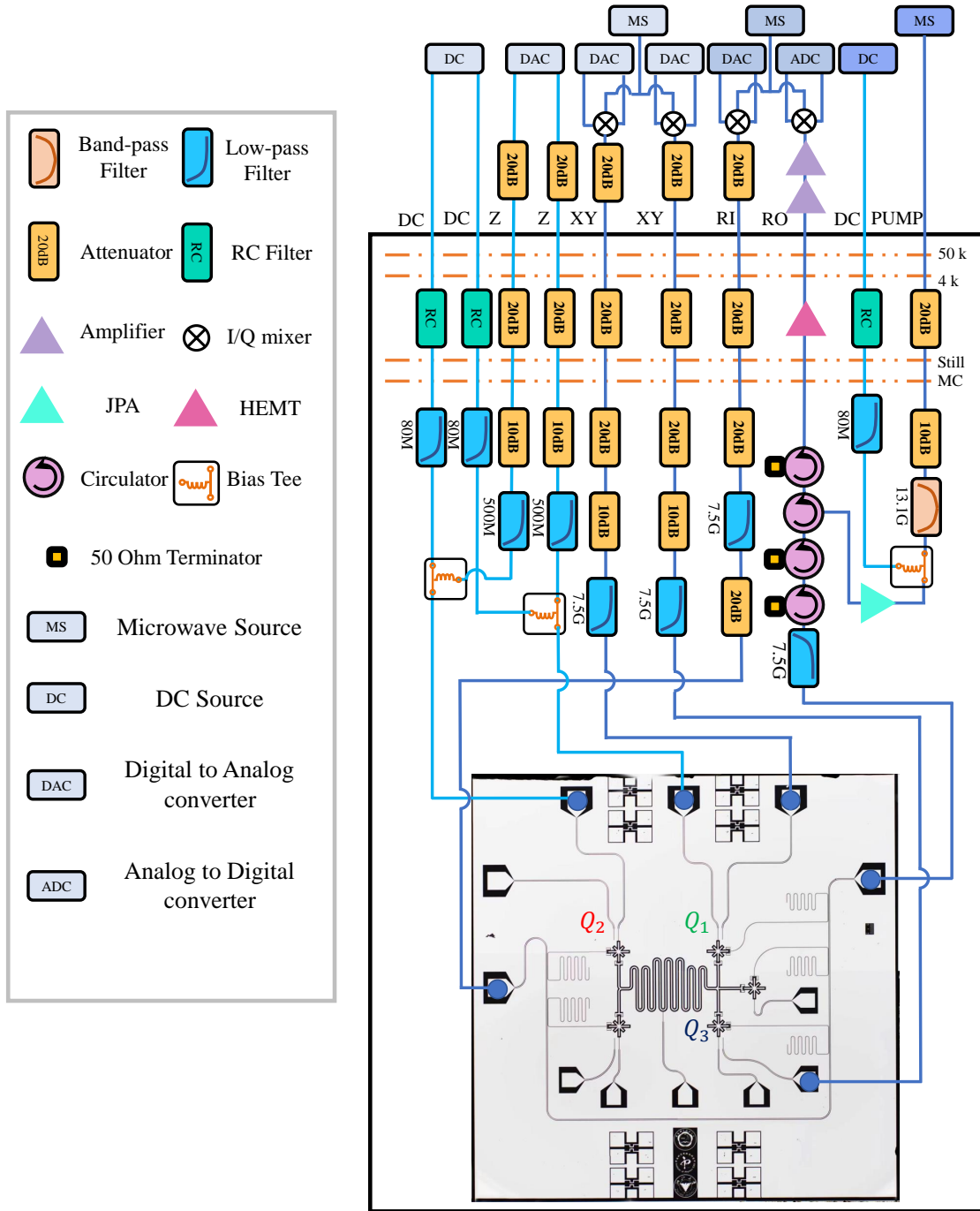


FIG. S1: Schematic diagram of the experimental setup. Note there is a low-pass filter (7.5G) inverted with the others because it connects to the read-out line.

a DC bias. Moreover, some circulators, attenuators, and filters are added to the signal lines in specific temperature regions to reduce the noises that influence the performance of the device.

Three of the five qubits are used in our experiment. One is used as the test qubit Q_1 for realizing the effective quantum Rabi model. The second one acts as an ancilla qubit Q_2 to determine the photon-number distribution for analyzing the Wigner function distribution whose negativity reveals and quantifies the nonclassicality of the light field. The XY-line of the third qubit Q_3 is used to control the bus resonator (by cross-talk interactions) for performing a displacement operation on its states in phase space.

The performance characterization of the qubits and the resonator are listed in Table S2. For technical details about

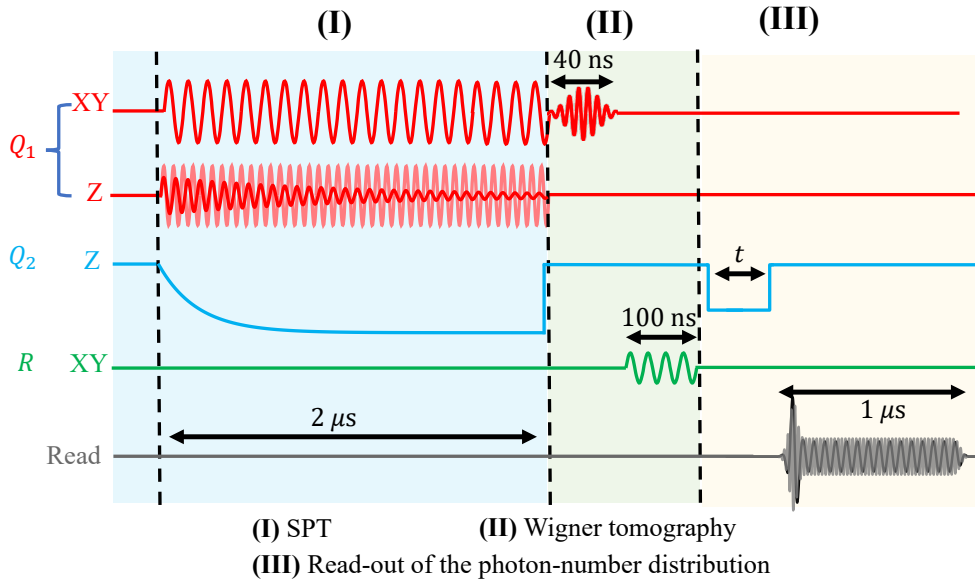


FIG. S2: Sketch of the pulse sequences, which consists of three steps: (I) superradiant phase transition (SPT); (II) Wigner tomography; and (III) read-out of the photon-number distribution. In (I), we apply a continuous drive pulse (amplitude $K/2\pi = 19.91$ MHz and frequency $\omega_0/2\pi = 5.18$ GHz) to the XY-line and two tunable pulses [$\varepsilon_1 \cos(\mu_1 t)$ and $\varepsilon_2 \cos(\mu_2 t)$, with $\{\varepsilon_1, \nu_1, \nu_2\}/2\pi = \{165.85, 200, 33.28\}$ MHz] to the Z-line of the test qubit Q_1 , where the amplitude of the second modulation pulse, ε_2 , slowly decreases with time, corresponding to the decrease of $\Omega(t)$. Moreover, the frequency $f(t)$ of the ancilla qubit Q_2 decreases with the amplitude of the Z-line, inducing a decrease in the $\delta(t)$ by Stark shifts. In (II) a single-qubit rotation operation [the identity operation, $R_x(\pi/2)$, or $R_y(\pi/2)$] is applied to the test qubit, and a displacement operation $D(-\beta)$ is then applied to the resonator (actually by tuning the XY-line of Q_3 with cross-talk interactions, not shown). In (III) the ancilla qubit Q_2 is resonantly coupled to the resonator for a given time τ , and then biased to its idle frequency ($f_{\text{idle}}/2\pi = 5.93$ GHz) for state read-out.

	$\omega_{10}/2\pi$ (GHz)	T_1 (μs)	T_2^* (μs)	T_2^{SE} (μs)	$\lambda/2\pi$ (MHz)	$\gamma/2\pi$ (MHz)	F_g	F_e
Q_1	5.180	21.5	1.1	6.0	19.91	250	0.983	0.937
Q_2	5.930	17.2	1.5	14.3	20.92	238	0.990	0.920
R	5.581	12.9	234.5	-	-	-	-	-

TABLE S2: **Qubit and resonator characteristics.** The symbols Q_1 , Q_2 , and R correspond to the test qubit, the ancilla qubit, and the resonator, respectively. The idle frequencies of Q_j ($j = 1, 2$) and R are generally marked by $\omega_{10}/2\pi$, where single-qubit rotation pulses and measurements are applied. For the decoherence performance, T_1 and T_2^* are the energy relaxation time and the Ramsey dephasing time (Gaussian decay), respectively, of Q_j and R , measured at the idle frequency. Additionally, T_2^{SE} is the dephasing time with spin echo (Gaussian decay). The coupling strength λ between Q_j and the bus resonator R is estimated via vacuum Rabi oscillations. The anharmonicity of the qubit is γ . The probability of detecting the qubit in $|g\rangle$ ($|e\rangle$) when it is prepared in $|g\rangle$ ($|e\rangle$) state is indicated by F_g (F_e).

the superconducting qubits, e.g., see Ref. [S4], which reports similar control methods to our experiment.

The pulse sequences are shown in Fig. S2, including three steps: (I) SPT; (II) Wigner tomography; and (III) read-out of the photon-number distribution. Because the time span of several operations varies widely, real scales are not used.

S3. CONTROL OF QUENCHING DYNAMICS

A. Time-dependence of the normalized coupling parameter ξ

During the quenching process, the normalized coupling parameter is changed as [S5]

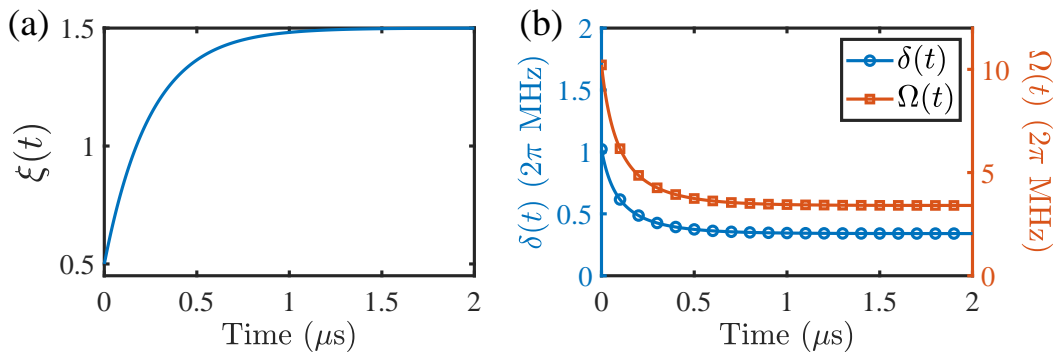


FIG. S3: (a) Normalized coupling parameter $\xi(t)$ versus time. (b) Effective frequencies $\delta(t)$ and $\Omega(t)$ of the resonator and qubit versus time, showing on the left and right y -axes, respectively.

$$\xi(t) = (\xi_{\max} - \xi_0) \left[1 - \exp\left(-\frac{8t}{t_f}\right) \right] + \xi_0. \quad (\text{S20})$$

Here, ξ_{\max} (ξ_0) is the maximum (initial) value of $\xi(t)$ and t_f is the total evolution time. For Figs. 2 and 3 in the main text, we choose $\xi_{\max} = 1.5$, $\xi_0 = 0.5$, and $t_f = 2 \mu\text{s}$. In addition, we choose $\Omega = 10\delta$ at all times of the evolution to ensure the preset limitation $\Omega \gg \delta$ of the SPT [S1]. The induced $\xi(t)$, $\Omega(t)$, and $\delta(t)$ are shown in Fig. S3.

The experiment starts by tuning the test qubit to the operating frequency $\omega_0/2\pi = 5.18$ GHz, around which the two sine modulations are applied, with the fixed modulation frequencies $\nu_1/2\pi = 200$ MHz and $\nu_2/2\pi = 33.28$ MHz. The amplitude of the first modulation is set to $\varepsilon_1/2\pi = 165.85$ MHz, while ε_2 is taken as a control parameter. Near the operating frequency, the qubit is driven by a continuous microwave with Rabi frequency $K/2\pi = 19.91$ MHz. For these settings, the dynamics of the test qubit and the resonator are governed by the Rabi Hamiltonian, with the qubit working in the frame rotating at the angular frequency B_0 relative to the laboratory frame. The resulting effective qubit-resonator coupling strength is $\eta/2\pi = 0.81$ MHz. During the Rabi dynamics, the ancilla qubit Q_2 is far off-resonant with the test qubit Q_1 and with the resonator, so that it remains in the ground state.

B. Control of the effective qubit frequency Ω

Because of the imperfect waveform of the periodically modulated excitation energy $\hbar\omega_q(t)$, we modify the first and second modulating pulses as $\varepsilon_1 \cos(\nu_1 t + \phi_1^{\text{exp}})$ and $\varepsilon_2 \cos(\nu_2 t + \phi_2^{\text{exp}})$, respectively, to optimize the most appropriate dynamics of the Rabi Hamiltonian H_R . We iterate over different phases ($\phi_1^{\text{exp}}, \phi_2^{\text{exp}}$) to carry out the experiments with setting $\delta = 0$, and finally obtain the one which best coincides with the corresponding simulated Rabi oscillation curves. The optimal results, specifically, for $\Omega/2\pi = 3.6$ MHz, are shown in Fig. S4, where we can see that the fitting error (the Euclidean norm) becomes minimal when $\phi_1^{\text{exp}} = 1.06\pi$ and $\phi_2^{\text{exp}} = 1.00\pi$. In this case, the concrete fitting situation is indicated in Fig. S5. The experimental data are intuitively close to the numerical fitting in Fig. S5, confirming the validity of such phase modification.

For convenience, we choose the same phase modifications (i.e., $\phi_1^{\text{exp}} = 1.06\pi$ and $\phi_2^{\text{exp}} = 1.00\pi$) for different Ω throughout the experiments. Note that we also slightly adjust the center frequencies and amplitudes of the two modulating pulses to improve the control.

C. Control of the effective resonator frequency δ

The control of the effective resonator frequency $\delta(t)$ of the effective Rabi Hamiltonian in Eq. (S9) can be achieved by adjusting the Stark shift induced by the ancilla qubit Q_2 . We can control this Stark shift by tuning the frequency of the ancilla qubit. When the detuning $\Delta\omega$ between this ancilla qubit and the resonator is varied from $\Delta\omega$ to $\Delta\omega'$, and remains much larger than their coupling strength λ' , the resulting resonator frequency shift becomes

$$\delta\omega_S = \frac{\lambda'^2}{\Delta\omega} - \frac{\lambda'^2}{\Delta\omega'}, \quad (\text{S21})$$

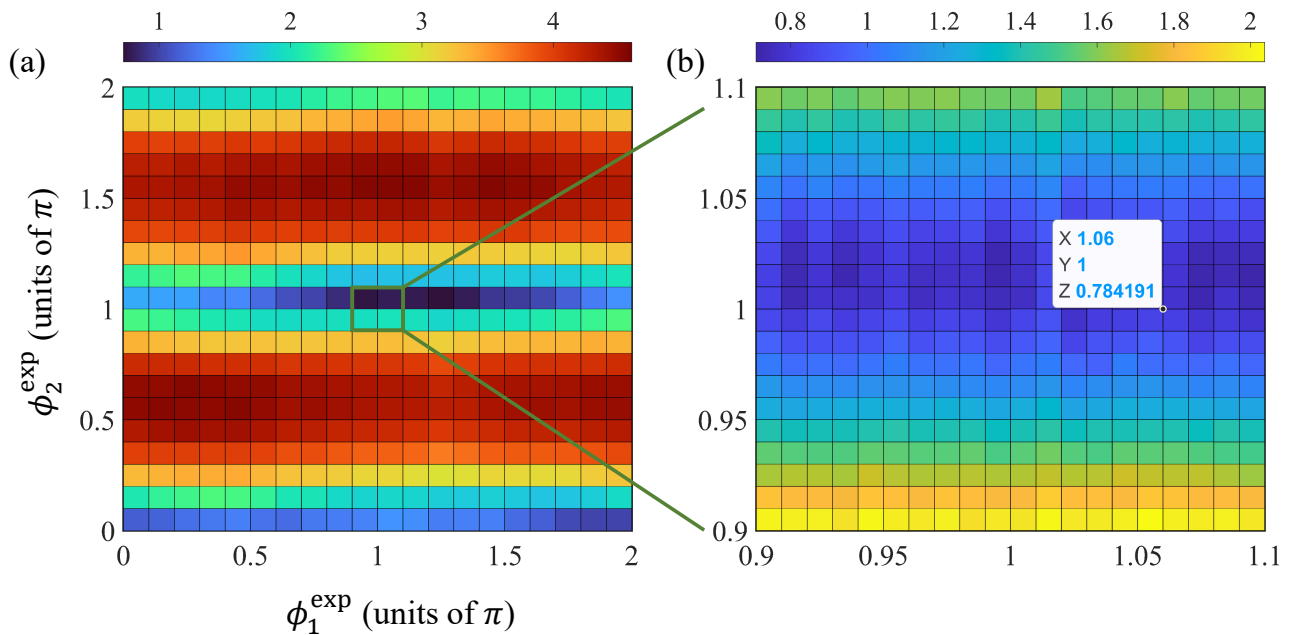


FIG. S4: (a) Fitting errors (Euclidean norm) versus phase modifications (ϕ_1^{exp} and ϕ_2^{exp}) in the experiment. (b) Magnified view of (a) when $\{\phi_1^{\text{exp}}, \phi_2^{\text{exp}}\} = [0.9, 1.1]\pi$, where the optimal point used in the experiment has been marked.

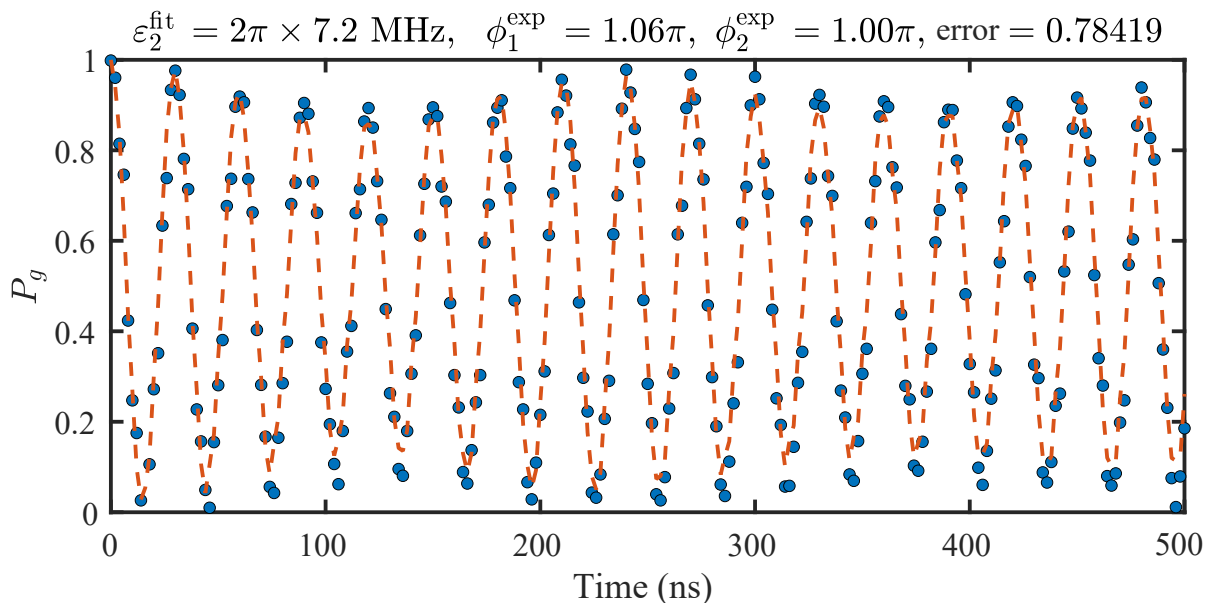


FIG. S5: Fitting for $\phi_1^{\text{exp}} = 1.06\pi$ and $\phi_2^{\text{exp}} = 1.00\pi$. The populations P_g in the ground state of the test qubit Q_1 versus time. The experiment data and the numerical results are marked by dots and a dashed curve, respectively.

where $\lambda'/2\pi = 20.91$ MHz (different from λ in the main text). Equation (S21), in a different form, reads

$$\delta(t) - \delta(0) = \frac{\lambda'^2}{f(0) - \omega_p} - \frac{\lambda'^2}{f(t) - \omega_p}, \quad (\text{S22})$$

with $f(t)$ being the transition frequency of the ancilla qubit. Based on Eq. (S22), we change $f(t)$ from the idle frequency f_{idle} , viz., $f(0)/2\pi = f_{\text{idle}}/2\pi = 5.93$ GHz, yielding,

$$f(t) = \omega_p - \left[\frac{\delta(t) - \delta(0)}{\lambda'^2} - \frac{1}{f_{\text{idle}} - \omega_p} \right]^{-1}. \quad (\text{S23})$$

To demonstrate the effectiveness of controlling $\delta(t)$ experimentally, we apply square pulses with amplitudes $f(t)$ (x -axis) to the Z-line of the ancilla qubit Q_2 . Meanwhile, several square-envelope pulses with certain amplitudes and specific frequencies $\omega_p + \delta(t)$ (y -axis) are applied to the XY-line of the test qubit Q_1 to excite the resonator (by cross-talk interactions). Subsequently, we measure the populations of the ancilla qubit Q_2 (z -axis) after a qubit-resonator-swap interaction (span time π/λ'). This spectroscopy reflects the relationship between applying $f(t)$ and the induced offset of the effective resonator frequency $\delta(t)$. After appropriately translating the y -axis and remapping values of $f(t)$ to the corresponding time, we achieve the experimental control of $\delta(t)$ as shown in Fig. S6, where the high-value populations (highlighted area) roughly depict the trend of the experimental $\delta(t)$ and coincide well with its ideal values.

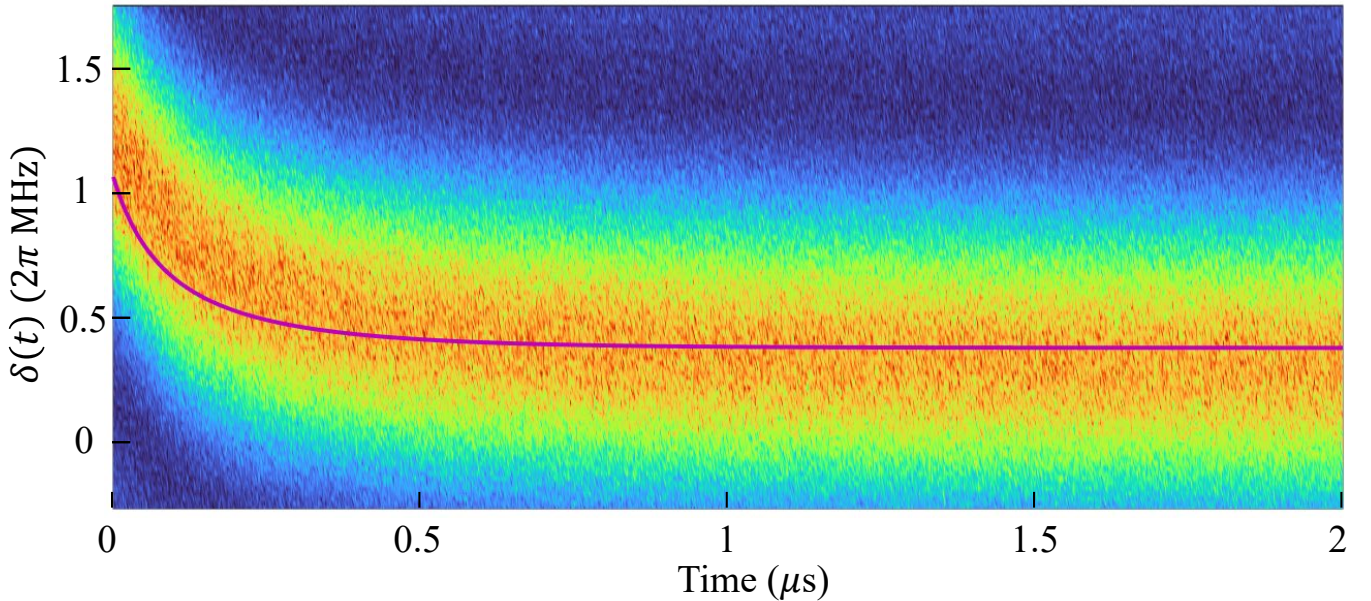


FIG. S6: Experimental frequency $\delta(t)$ of the resonator versus time, induced by tuning the frequency of the ancilla qubit Q_2 with a suitable translation added to the y -axis. The ideal $\delta(t)$ is plotted with a solid purple-solid curve.

S4. EFFECTS OF OFF-RESONANT COUPLINGS AND DECOHERENCE

When considering high-energy levels of the Xmon qubit, the Hamiltonian becomes

$$H = H_0 + H_I, \quad (\text{S24})$$

$$H_0 = (\omega_0 + 2\nu_1)a^\dagger a + [\omega_0 + \varepsilon_1 \cos(\nu_1 t)]q^\dagger q - \frac{\gamma}{2}q^{\dagger 2}q^2, \quad (\text{S25})$$

$$H_I = \delta a^\dagger a + (\lambda a^\dagger q + \text{h.c.}), \quad (\text{S26})$$

where q (q^\dagger) denotes the annihilation (creation) operator for the Xmon qubit mode and γ is the anharmonicity of the qubit. For simplicity, we ignore the microwave driving K and the frequency modulation ε_2 . Performing the transformation U_0 and considering the lowest three levels of the Xmon qubit, $\{|g\rangle, |e\rangle, |f\rangle\}$, we obtain the system Hamiltonian in the rotating frame as

$$H'_I = \delta a^\dagger a + \left\{ \exp[-i\mu \sin(\nu_1 t)] \lambda \exp(2i\nu_1 t) a^\dagger [|g\rangle \langle e| + \sqrt{2} \exp(i\gamma t) |e\rangle \langle f|] + \text{h.c.} \right\}. \quad (\text{S27})$$

Using the Jacobi-Anger expansion, we obtain

$$H'_I = \delta a^\dagger a + \left(\sum_{n=-\infty}^{\infty} J_n(\mu) \lambda a^\dagger \left\{ \exp[-i(n-2)\nu_1 t] |g\rangle \langle e| + \sqrt{2} \exp[-i(n-2)\nu_1 t + i\gamma t] |e\rangle \langle f| \right\} + \text{h.c.} \right). \quad (\text{S28})$$

By assuming that $\{|\lambda J_0(\mu)|, \delta\} \ll \nu_1$, H'_I reduces to the effective Hamiltonian

$$H_e = [J_2(\mu) \lambda a^\dagger] |g\rangle \langle e| + \text{h.c.} \\ + S_1(|g\rangle \langle g| - |e\rangle \langle e|) a^\dagger a - S_1 |e\rangle \langle e| + S_2 |e\rangle \langle e| a^\dagger a + \delta a^\dagger a, \quad (\text{S29})$$

where

$$S_1 \simeq \frac{[J_0(\mu)\lambda]^2}{2\nu_1} + \frac{[J_1(\mu)\lambda]^2}{\nu_1} + \frac{[J_{-1}(\mu)\lambda]^2}{3\nu_1}, \quad (\text{S30})$$

$$S_2 \simeq \frac{2[J_0(\mu)\lambda]^2}{2\nu_1 + \gamma} + \frac{2[J_1(\mu)\lambda]^2}{\nu_1 + \gamma} + \frac{2[J_{-1}(\mu)\lambda]^2}{3\nu_1 + \gamma}. \quad (\text{S31})$$

The term $S_2 |e\rangle \langle e| a^\dagger a$ results from a dispersive coupling to the second-excited state $|f\rangle$.

Discarding the constant term, we can rewrite H_e as

$$H_e = H_{e,1} + H_{e,2}, \quad (\text{S32})$$

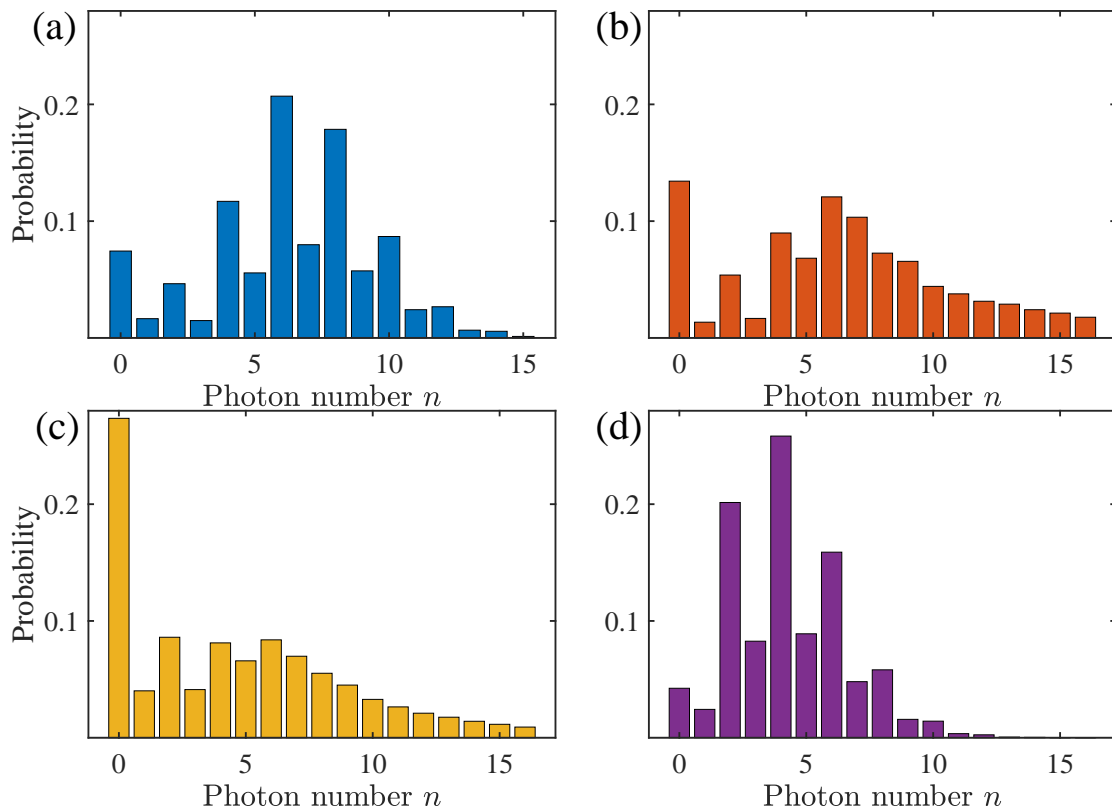


FIG. S7: Numerically simulated photon-number distributions of fields at $t = 2 \mu\text{s}$, which are calculated by the (a) effective Hamiltonian without decoherence, (b) full Hamiltonian without decoherence, and (c) full Hamiltonian with decoherence. (d) Ground state results of the effective Hamiltonian.

where

$$H_{e,1} = [J_2(\mu)\lambda a^\dagger] |g\rangle \langle e| + \text{h.c.}, \quad (\text{S33})$$

$$H_{e,2} = \left(S_1 - \frac{1}{2}S_2\right) (|g\rangle \langle g| - |e\rangle \langle e|) a^\dagger a + \frac{1}{2}S_1 (|g\rangle \langle g| - |e\rangle \langle e|) + \left(\frac{1}{2}S_2 + \delta\right) a^\dagger a. \quad (\text{S34})$$

Therefore, the Stark shifts are significantly reduced when the effect of the second-excited state $|f\rangle$ is considered. For the present device parameter setting, we obtain

$$S_1 - \frac{1}{2}S_2 \sim 2\pi \times 0.45 \text{ MHz}. \quad (\text{S35})$$

When the microwave drive is applied, $H_{e,2}$ becomes

$$H'_{e,2} = \frac{(S_1 - \frac{1}{2}S_2)^2}{2K} \sigma_x (a^\dagger a)^2 + \frac{(\frac{1}{2}S_1)^2}{2K} \sigma_x + \left(\frac{1}{2}S_2 + \delta\right) a^\dagger a, \quad (\text{S36})$$

where

$$\frac{(S_1 - \frac{1}{2}S_2)^2}{2K} \simeq \frac{2\pi \times 0.45^2}{40} \text{ MHz} = 2\pi \times 0.0061 \text{ MHz}. \quad (\text{S37})$$

The first term of Eq. (S36) produces a qubit-state-dependent Kerr effect on the photonic field, dispersing the phase-space distributions of the coherent fields, which partly accounts for distortions of the observed Gaussian wavepackets. To quantitatively explore influences arising from imperfect Hamiltonian dynamics and decoherence, we perform numerical simulations on the photon-number distributions at $t = 2 \mu\text{s}$. Figures S7(a) and S7(b) present results based on the effective Rabi Hamiltonian and the full Hamiltonian, respectively; while Fig. S7(c) displays the result calculated by the master equation, including both the full Hamiltonian dynamics and decoherence. Figure S7(d) shows the photon number distributions associated with the ground state of the effective Rabi Hamiltonian. For the ground state of the ideal Rabi model with an infinite frequency ratio [S1], the vacuum component has a negligible population. Due to the experimental imperfections, the observed output state has a significant vacuum population of about 0.29. To quantify individual contributions to the vacuum population, we perform numerical simulations step by step, including more and more experimental imperfections. Thus obtained vacuum populations are respectively 0.07, 0.13, 0.27, and 0.04, as shown in Figs. S7(a)-(d). The results imply that the limitation of the effective qubit-resonator frequency ratio, non-adiabaticity, deviation from model Hamiltonian, and dissipation contribute vacuum populations of 0.04, $0.07 - 0.04 = 0.03$, $0.13 - 0.07 = 0.06$, and $0.27 - 0.13 = 0.14$, respectively. We note the calculated vacuum population 0.27 in Fig. S7(c) is slightly smaller than the observed result 0.29 in Fig. 2 in the main text, mainly due to deviations of the system parameters used for the simulation from their real values. In the simulation, the dissipation times for the qubit and the resonator are the same as those listed in Table S2. These results clearly show that the population of the vacuum state is mainly caused by decoherence.

Note that there are also two corrections in the numerical simulation for the master equation: (i) applying $\Omega(t)' = 1.56 \Omega(t)$ [$\Omega(t)$ shown in Fig. S3]; (2) utilizing the fitting $\delta'(t)$ deduced by experimental measurements in Fig. S6, shown in Fig. S8.

The simulated average photon number has shown in Fig. 2 in the main text. Additionally, based on such numerical simulation, we plot the corresponding Wigner functions in Fig. S9. We also plot the population of the third level $|f\rangle$ in Fig. S10, when the $|f\rangle$ is included in the numerical simulation. The results show that the average population of the third level is about 0.11 during the quenching dynamics.

S5. CHARACTERIZATION OF THE QUBIT-RESONATOR STATE

A. Photon-number distribution

All the measured average photon numbers and the Wigner function values in the main text are deduced from the photon-number distribution. In the experiment, after carrying out the part of the SPT (or after Wigner tomography),

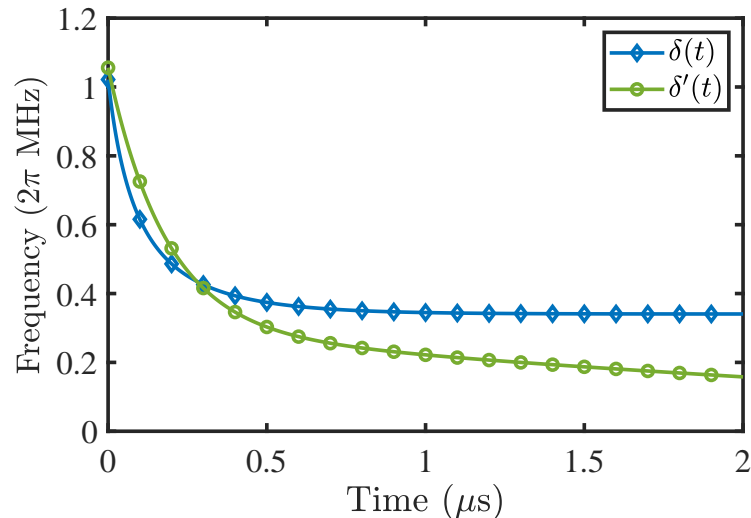


FIG. S8: Effective resonator frequency versus time. The green line with circular markers represents the fitting effective resonator frequency $\delta'(t)$ deduced by experimental measurements in Fig. S6. The blue line with diamond markers indicates the ideal effective resonator frequency.

the microwave drive K and the frequency modulations ω_g are switched off. Meanwhile, the ancilla qubit Q_2 is tuned on resonance with the resonator (frequency 5.581 GHz) from the idle frequency 5.93 GHz. Furthermore, the ancilla qubit Q_2 undergoes photon-number-dependent Rabi oscillations. The populations $P_e^a(\tau)$, of the excited state of the ancilla qubit Q_2 for a given interaction time τ , are measured by biasing the ancilla back to its idle frequency, where its state is read out (intuitively see Fig. S2). The recorded time-resolved quantum Rabi oscillation signals can be fitted as

$$P_e^a(\tau) = \frac{1}{2} \left[1 - P_g^a(0) \sum_{n=0}^{n_{\max}} P_n e^{-\kappa_n \tau} \cos(2\sqrt{n}\lambda'\tau) \right], \quad (\text{S38})$$

where P_n denotes the photon-number distribution probability, $P_g^a(0)$ indicates the probability for the ancilla qubit Q_2 to start in the ground state, n_{\max} is the cutoff of the photon number, and $\kappa_n = n^l/T_{1,p}$ ($l = 0.7$) [S6–S10] is the empirical decay rate of the Rabi oscillations associated with the n -photon state. It is worth mentioning that, when there are a lot of photons in the resonator, especially $\langle a^\dagger a \rangle > 10$, the detuning $\Delta\omega/2\pi = (5.93 - 5.581)$ GHz = 0.329 GHz is not large enough to avoid interactions between the ancilla qubit Q_2 and the resonator. This induces a minor excitation of the ancilla qubit Q_2 , depending on the excitation of the resonator. Thus, referring to [S6], we ignore the small excitation of $|e\rangle$ and rescale the factor $1/2$ in the photon-number-dependent Rabi oscillations equation [S10], to $P_g(0)/2$ [see Eq. (S38)]. Based on the measurements and fitting operations described above, we can give the fitting situation and corresponding photon-number distribution in Fig. S11.

B. Diagonal Wigner matrix elements

As described in the main text, the Wigner function is given by

$$\mathcal{W}_{k,k'}(\beta) = \frac{2}{\pi} \sum_{n=0}^{\infty} (-1)^n \mathcal{P}_n^{k,k'}(\beta), \quad (\text{S39})$$

where

$$\mathcal{P}_n^{k,k'}(\beta) = \langle n | D(-\beta) \rho_{k,k'} D(\beta) | n \rangle. \quad (k, k' = e, g)$$

To measure the Wigner diagonal elements, a displacement operation, $D(\beta) = \exp(\beta a^\dagger - \beta^* a)$, is applied to the resonator, following which the ancilla qubit Q_2 is resonantly coupled to the resonator for a given time τ . Then, the ancilla qubit Q_2 is biased to the idle frequency for the read-out of states.

The photon-number distributions $\mathcal{P}_n^{g,g}(\beta)$ and $\mathcal{P}_n^{e,e}(\beta)$ of the displaced light field are associated with the test qubit states $|g\rangle$ and $|e\rangle$. Such distributions can be extracted from the excited-state populations $[P_{n,e}^g(\beta, \tau)$ and $P_{n,e}^e(\beta, \tau)]$ of the ancilla qubit, conditional on the detection of the test qubit in states $|g\rangle$ and $|e\rangle$. Thus, the normalized Wigner function (for diagonal elements in the qubit basis) is given by

$$W_{k,k}(\beta) = \mathcal{W}_{k,k}(\beta)/P_k, \quad (\text{S40})$$

with P_k being the $|k\rangle$ -state population of the test qubit. To completely show the distribution of the generated cat states in phase space, we calibrate $\{\text{Re}(\beta), \text{Im}(\beta)\} \in [-3, 3]$, implying that the displacement distance of $D(-\beta)$, i.e., $|\beta|$, can be up to $3\sqrt{2}$. This leads to the fact that the displaced light fields in some cases process an average photon number $\langle a^\dagger a \rangle \gtrsim 18$.

However, as claimed in Sec. S5 A, the read-out of the photon-number distribution becomes imprecise with photons growing. We therefore ignore the areas with large numbers of photons and utilize the remaining areas to deduce the normalized density matrix $\rho_{k,k}/P_k$ of light fields. This treatment is intuitively shown in Fig. S12. The calculation from the Wigner function $W_{k,k}(\beta)$ to the density matrix $\rho_{k,k}/P_k$ is completed using convex optimization, supported by

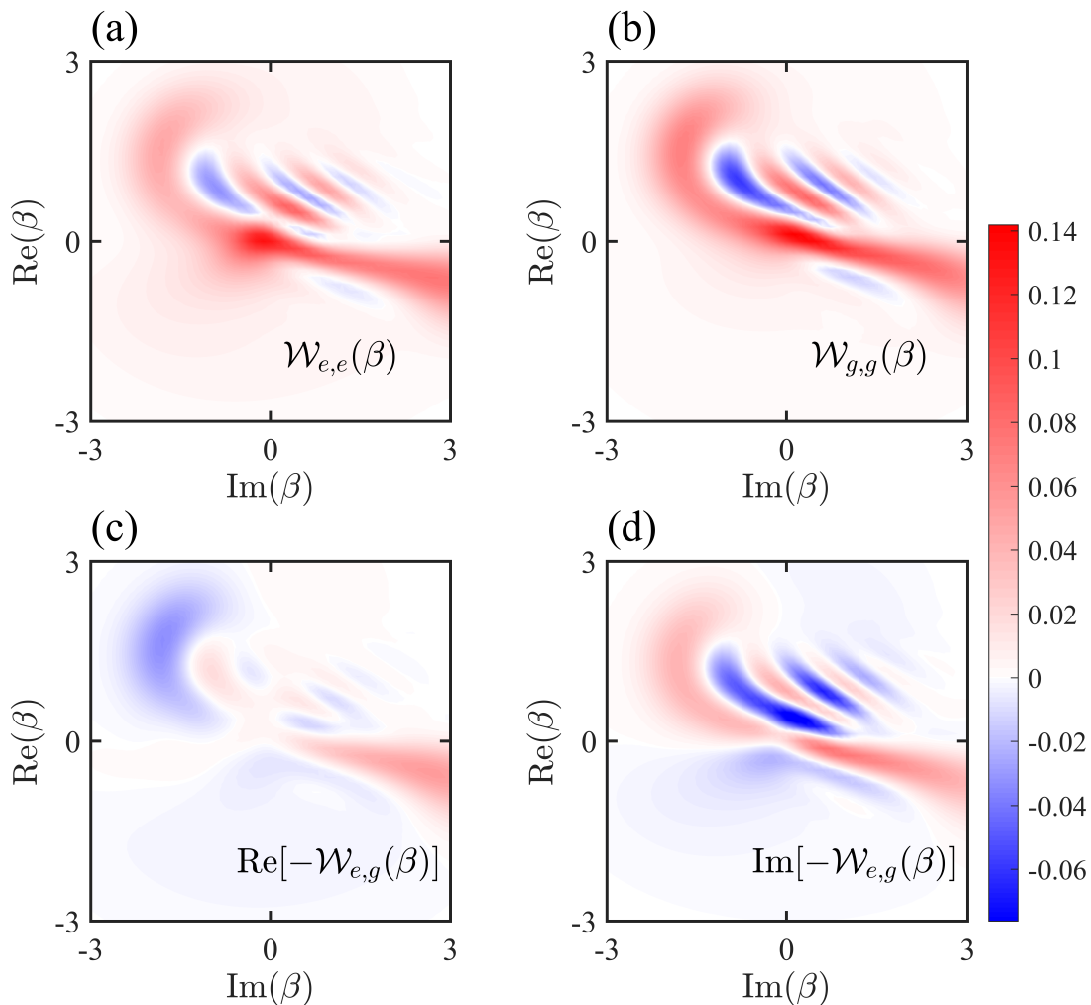


FIG. S9: Numerically simulated Wigner matrix tomography. (a–d) Corresponds to Fig. 3 (a–d) in the main text, respectively. Note that suitable rotations of Wigner tomography have been applied and all the data are measured at $t = 2 \mu\text{s}$ based on the parameter corrections in Sec. S4.

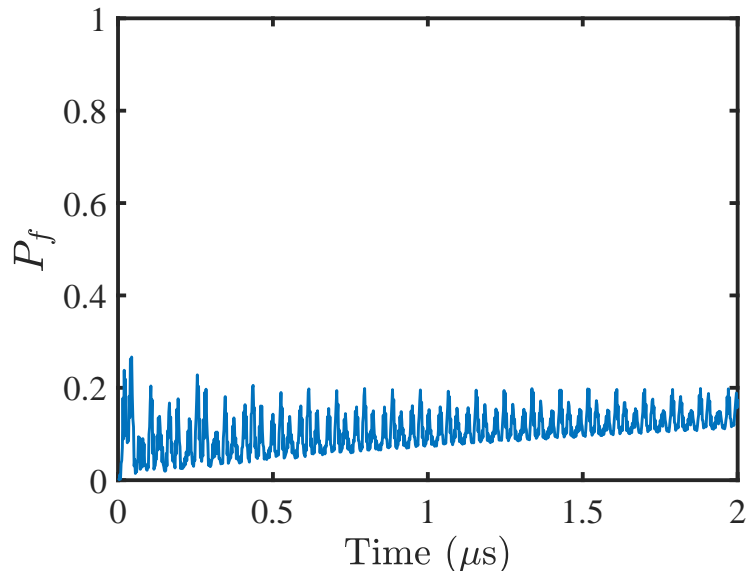


FIG. S10: Numerically simulated population of the third level $|f\rangle$.

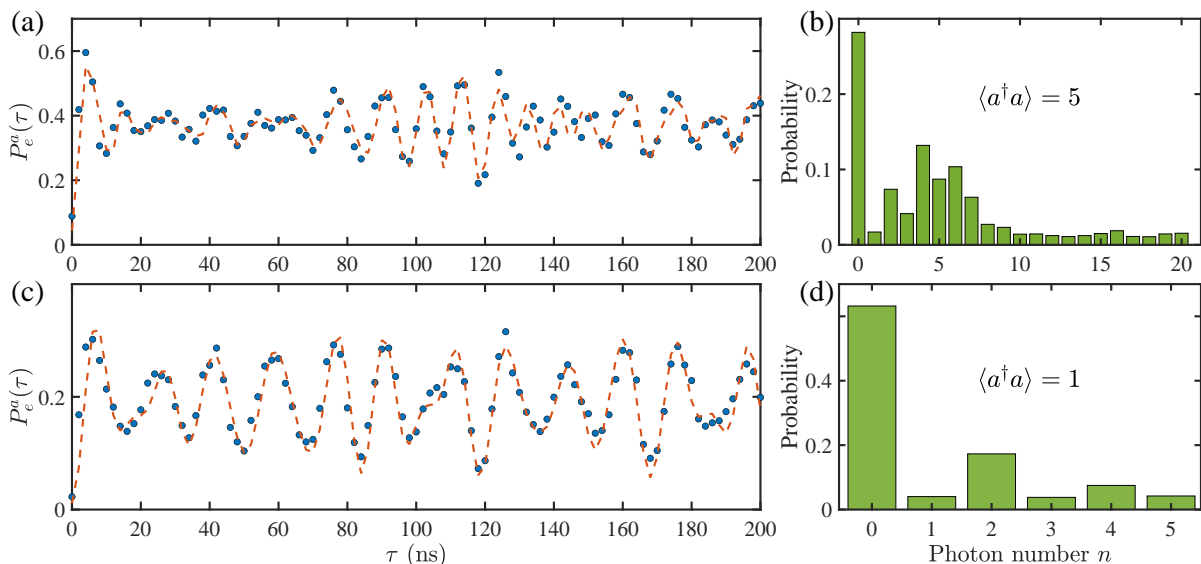


FIG. S11: Experimental (dots) and theoretical (dashed curves) time-resolved quantum Rabi oscillations and corresponding photon-number distributions for (a, b) $\langle a^\dagger a \rangle = 5$ and (c, d) $\langle a^\dagger a \rangle = 1$.

the CVX toolbox based on MATLAB [S11]. The solved density matrix $\rho_{k,k}/P_k$ is Hermitian and positive semidefinite as well as satisfying $\text{Tr}(\rho_{k,k}/P_k) = 1$. Furthermore, we use this solved $\rho_{k,k}/P_k$ to plot $\mathcal{W}_{k,k}(\beta)$, shown in Figs. 3(a) and 3(b) in the main text, which has the same distribution in phase space as Figs. S12(a) and S12(b) here. As for Figs. 3(c) and 3(d) in the main text, we additionally perform Wigner tomography (detailed in the next section) and take the same treatment as that for Figs. S12(a) and S12(b). The time to measure the Wigner function is $t=1.946 \mu\text{s}$ because the error of the qubit projection is relatively small at this time.

C. Off-diagonal Wigner matrix elements

To fully characterized the nonclassical light-matter correlations, it is necessary to reconstruct the off-diagonal elements, measurements of which require Wigner tomography in the rotated basis $\{|\pm_x\rangle = (|e\rangle \pm |g\rangle)/\sqrt{2}\}$ and

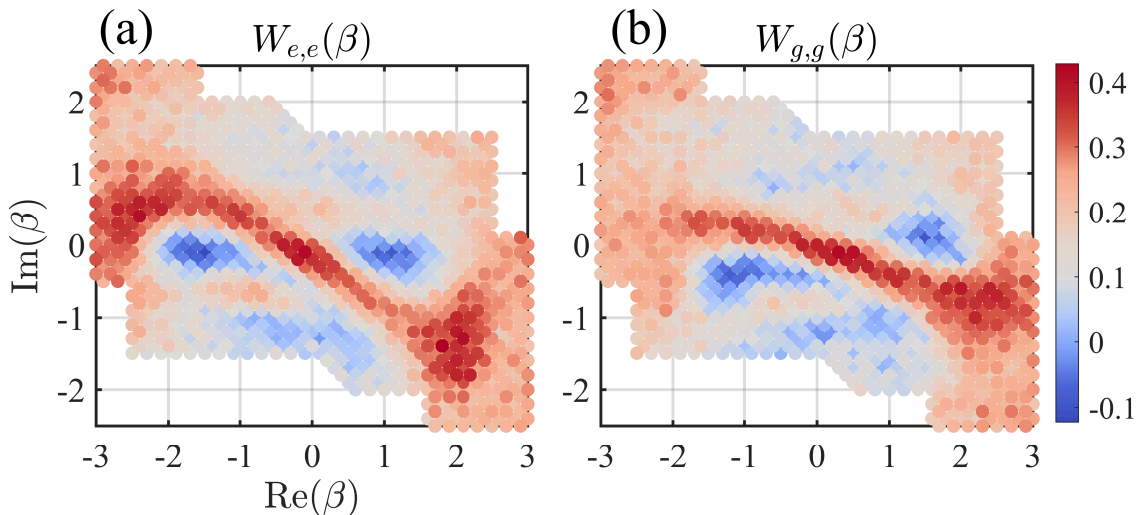


FIG. S12: Experimental data of the Wigner functions (a) $W_{e,e}(\beta)$ and (b) $W_{g,g}(\beta)$, without displaying the points corresponding to large numbers of photons ($\langle \hat{a}^\dagger \hat{a} \rangle > 10$).

$\{|\pm_y\rangle\} = (|e\rangle \pm i|g\rangle)/\sqrt{2}$, respectively. The Wigner diagonal elements in these bases are related to both diagonal and off-diagonal elements in the basis $\{|e\rangle, |g\rangle\}$:

$$\mathcal{W}_{\pm x, \pm x}(\beta) = \frac{1}{2}[\mathcal{W}_{e,e}(\beta) + \mathcal{W}_{g,g}(\beta)] \pm \text{Re}[\mathcal{W}_{e,g}(\beta)], \quad (\text{S41})$$

$$\mathcal{W}_{\pm y, \pm y}(\beta) = \frac{1}{2}[\mathcal{W}_{e,e}(\beta) + \mathcal{W}_{g,g}(\beta)] \mp \text{Im}[\mathcal{W}_{e,g}(\beta)]. \quad (\text{S42})$$

To measure the Wigner matrix element $\mathcal{W}_{+x,+x}(\beta)$, a rotation $R_y(\pi/2)$ is performed on the test qubit Q_1 before its state read-out, transforming the x -axis basis states $|+x\rangle$ and $|-x\rangle$ to the z -axis basis states $|e\rangle$ and $|g\rangle$, respectively, which can be directly measured by the read-out resonator. After this rotation and the resonator displacement $D(-\beta)$, the measured photon-number distribution $\mathcal{P}_n^{e,e}(\beta)$, conditional on the detection of the test qubit state $|e\rangle$, yields the conditional Wigner function $W_{+x,+x}(\beta)$. Similarly, performing the resonator displacement $D(-\beta)$ after a qubit rotation $R_x(\pi/2)$, we can reconstruct the conditional Wigner function $W_{+y,+y}$ based on the measured photon-number distribution $\mathcal{P}_n^{e,e}(\beta)$. The elements $\mathcal{W}_{\pm J, \pm J}(\beta)$ ($J = x, y$) are related to the normalized Wigner function $W_{\pm J, \pm J}(\beta)$ by

$$\mathcal{W}_{\pm J, \pm J}(\beta) = P_{\pm J}^{e(g)} W_{\pm J, \pm J}(\beta), \quad (\text{S43})$$

where $P_J^{e(g)}$ denotes the $|e\rangle, |g\rangle$ -state population of the test qubit Q_1 after the corresponding frame transformation. Moreover, the real and imaginary parts of the off-diagonal element $\mathcal{W}_{e,g}(\beta)$, can be calculated by

$$\begin{aligned} \text{Re}[\mathcal{W}_{e,g}(\beta)] &= \frac{1}{2}[\mathcal{W}_{+x,+x}(\beta) - \mathcal{W}_{-x,-x}(\beta)], \\ \text{Im}[\mathcal{W}_{e,g}(\beta)] &= \frac{1}{2}[\mathcal{W}_{-y,-y}(\beta) - \mathcal{W}_{+y,+y}(\beta)]. \end{aligned} \quad (\text{S44})$$

Note that $\mathcal{W}_{\pm x, \pm x}$ and $\mathcal{W}_{\pm y, \pm y}$ can be described the same as $\mathcal{W}_{k,k}$ in Sec. S5B. The images of $\text{Re}[-\mathcal{W}_{e,g}(\beta)]$ and $\text{Im}[\mathcal{W}_{e,g}(\beta)]$ are shown in Figs. 3(c) and 3(d) in the main text, respectively.

S6. MEASURE OF THE QUBIT-RESONATOR ENTANGLEMENT

The partial transpose of the density matrix is

$$\rho^{\Gamma_Q} = \sum_{k=e,g} \sum_{k'=e,g} \rho_{k',k} \otimes |k\rangle\langle k'|, \quad (\text{S45})$$

whose eigenvalues are defined as E_i . The negativity [S12] is the absolute sum of the negative eigenvalues, viz., $\mathcal{N}(\rho) = |\sum_{E_i < 0} E_i| = 0.2483$. For comparison, the upper bound of the negativity, is $\mathcal{N}(|\psi_{\text{sp}}\rangle\langle\psi_{\text{sp}}|) = 0.4483$. The difference between the experimental negativity and the ideal one is mainly due to the influence of decoherence, demonstrated by the loss of the purity of the density matrix from 1 to 0.4646.

S7. CHARACTERIZATION OF THE SUPER-CAT STATE

Due to the non-adiabatic effects and the presence of decoherence, the emergent cat state during the SPT contains three superimposed components: one corresponding to the empty field mode, while the other two corresponding to the emergent coherent fields with opposite phases, as illustrated in Fig. S13. The size of this super-cat state is given by

$$\mathcal{S} = \frac{\sum_{s \neq l} d_{sl}^2 \sqrt{P_s P_l}}{\sum_{s \neq l} \sqrt{P_s P_l}}, \quad (\text{S46})$$

with $\{s, l\} = \{|0\rangle, |\alpha\rangle, |-\alpha\rangle\}$ and d_{sl}^2 indicating the square of the phase-space distance between s and l . Here $P_{|0\rangle}$, $P_{|\alpha\rangle}$, and $P_{|-\alpha\rangle}$ are the populations in $|0\rangle$, $|\alpha\rangle$, and $|-\alpha\rangle$ of $\rho_{e,e}/\text{Tr}(\rho_{e,e})$ [or $\rho_{g,g}/\text{Tr}(\rho_{g,g})$], respectively. For the three-components cat-like state, mixing $|0\rangle$, $|\alpha\rangle$, and $|-\alpha\rangle$, Eq. (S46) becomes

$$\mathcal{S} = \frac{\sqrt{P_{|0\rangle} P_{|\alpha\rangle}} |\alpha|^2 + \sqrt{P_{|0\rangle} P_{|-\alpha\rangle}} |\alpha|^2 + \sqrt{P_{|\alpha\rangle} P_{|-\alpha\rangle}} |2\alpha|^2}{\sqrt{P_{|0\rangle} P_{|\alpha\rangle}} + \sqrt{P_{|0\rangle} P_{|-\alpha\rangle}} + \sqrt{P_{|\alpha\rangle} P_{|-\alpha\rangle}}}, \quad (\text{S47})$$

specifically, $\mathcal{S}_{e,e} = 14.03$ and $\mathcal{S}_{g,g} = 13.27$ for $\rho_{e,e}/\text{Tr}(\rho_{e,e})$ and $\rho_{g,g}/\text{Tr}(\rho_{g,g})$, respectively.

The NP-SP quantum coherences associated with the qubit states $|e\rangle$ and $|g\rangle$ are

$$\mathcal{C}_{e,e} = \sum_{n=1}^{\infty} |\langle 0 | \rho_{e,e} | n \rangle| / \text{Tr}(\rho_{e,e}) = 1.018, \quad \text{and} \quad \mathcal{C}_{g,g} = \sum_{n=1}^{\infty} |\langle 0 | \rho_{g,g} | n \rangle| / \text{Tr}(\rho_{g,g}) = 1.020, \quad (\text{S48})$$

respectively. The quantum coherence averaged over these two super-cat states is 1.019.

Negative values of the Wigner functions clearly distinguish cat states, which are macroscopically-distinct coherent superpositions of classical-like states, from their mixtures. These negative values (as shown by the blue regions in Figs. S9 and S12, as well as Fig. 3 in the main text), which are clearly seen between the main peaks (as shown on the left- and right-hand sides of the figures), occur as a result of interference in the phase space [S13]. In the digital quantum simulation of the deep-strong coupling dynamics reported in Ref. [S14], a similar nonclassical state was generated by repetitive application of digital π pulses interleaved with short Jaynes-Cummings (JC) interaction without the counter-rotating-wave terms, which allows emulation of the long-time Rabi dynamics, but does not lead to the simultaneous realization of the JC and anti-JC interactions necessary for observing the associated SPT.

S8. NUMERICAL SIMULATION OF THE DICKE-MODEL SPT

Pushing one step further, we theoretically extend our method to the Tavis-Cummings (TC) model involving multiple qubits coupled to a resonator [S15, S16]. By longitudinally modulating and transversely driving each qubit, the TC model can be effectively transformed to the Dicke model with similar parameters. The results show that the qubits-resonator system can be evolved from the NP to the SP featuring a highly entangled cat state, formed by two photonic coherent states with opposite phases that are nonclassically correlated with distinct multiqubit coherent states also with opposite phases.

The Dicke model, composed of N qubits coupled to a quantum photonic field mode, is described by the Hamiltonian

$$H_D = \delta a^\dagger a + \sum_{j=1}^N \left[\frac{\Omega}{2} (|e_j\rangle\langle e_j| - |g_j\rangle\langle g_j|) \right]$$

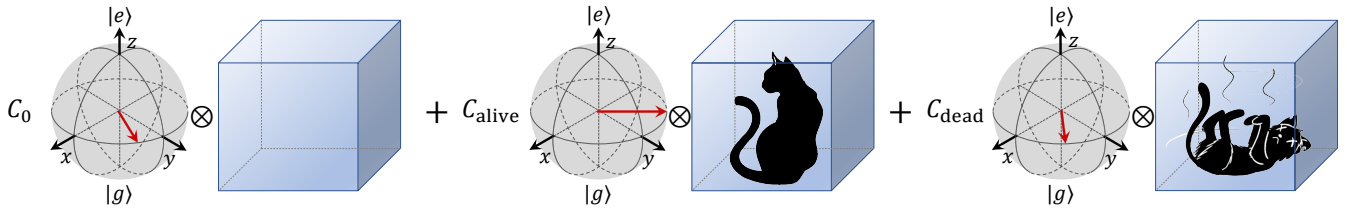


FIG. S13: Pictorial illustration of the three-component cat state. The resonator is in a superposition of being empty (without any cat) and containing a coherent field, which is formed by two superimposed components with complex amplitude α (alive cat) and $-\alpha$ (dead cat). These field components are correlated with different Bloch vectors (red-arrow lines) of the qubit.

$$+ \frac{\eta}{\sqrt{N}} (|e_j\rangle \langle g_j| + |g_j\rangle \langle e_j|)(a^\dagger + a), \quad (\text{S49})$$

where η denotes the collective qubit-field coupling strength, and $|g_j\rangle$ and $|e_j\rangle$ denoting the ground and excited states of the j th qubit, respectively. In the thermal limit $N \rightarrow \infty$, the system undergoes a SPT at the critical point $\xi = 2\eta/\sqrt{\Omega\delta} = 1$ [S17]. When ξ is sufficiently large the system has two degenerate ground states, given by [S18]

$$|\psi_{sp}^\pm\rangle \simeq \frac{1}{\sqrt{2}} [|\alpha'\rangle \prod_{j=1}^N |+_j\rangle \pm |-\alpha'\rangle \prod_{j=1}^N |-_j\rangle], \quad (\text{S50})$$

where $|\pm_j\rangle = (|g_j\rangle \pm |e_j\rangle)/\sqrt{2}$, and $|\pm\alpha'\rangle$ represent the coherent states of the photonic field, with $\alpha' = \frac{\sqrt{N}\lambda}{\delta} \sqrt{1 - \xi^{-2}}$. For the even-parity ground state $|\psi_{sp}^+\rangle$, the field parts associated with the even and odd collective excitation numbers of the qubits are even and odd cat states, $|C_\pm\rangle = (|\alpha'\rangle \pm |-\alpha'\rangle)/\sqrt{2}$, respectively.

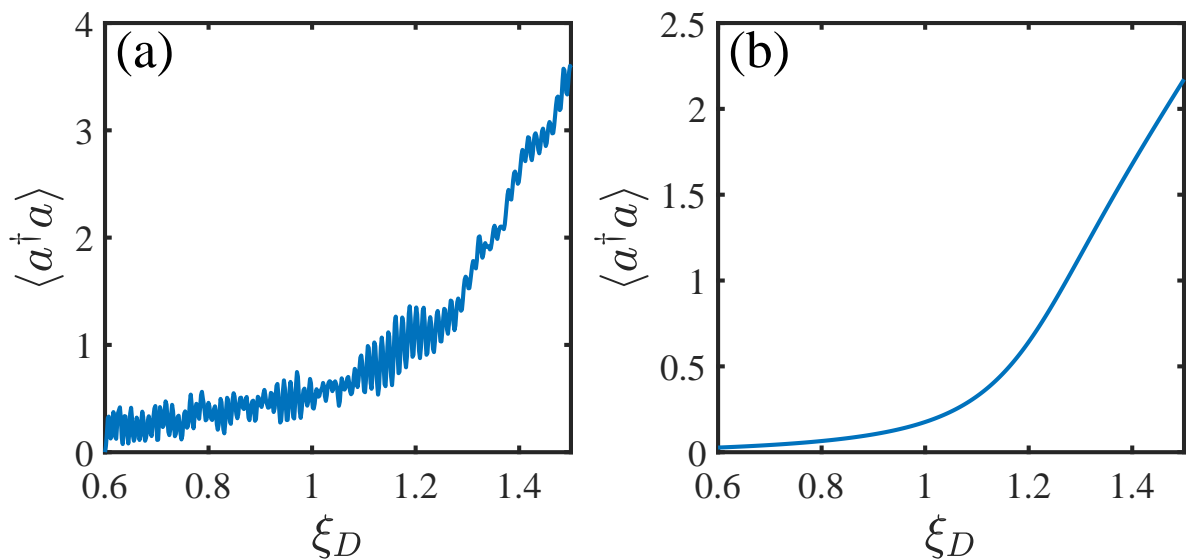


FIG. S14: Numerically simulated average photon number. (a) Result governed by full Hamiltonian. (b) Result deduced by even ground state of the Dicke-model Hamiltonian.

When the coupling strength λ between each qubit and the resonator is much smaller than the qubits' frequency ω_0 and the field frequency ω_p , the counter-rotating-wave terms for realizing the Dicke SPT can be effectively realized by applying a resonant transverse driving with the amplitude K , and two longitudinal modulations with frequencies ν_1 and ν_2 and amplitudes ε_1 and ε_2 , to each of the qubit. Under the conditions $\lambda, K, \delta = \omega_p - \omega_0 - 2\nu_1 \ll \nu_1$ and

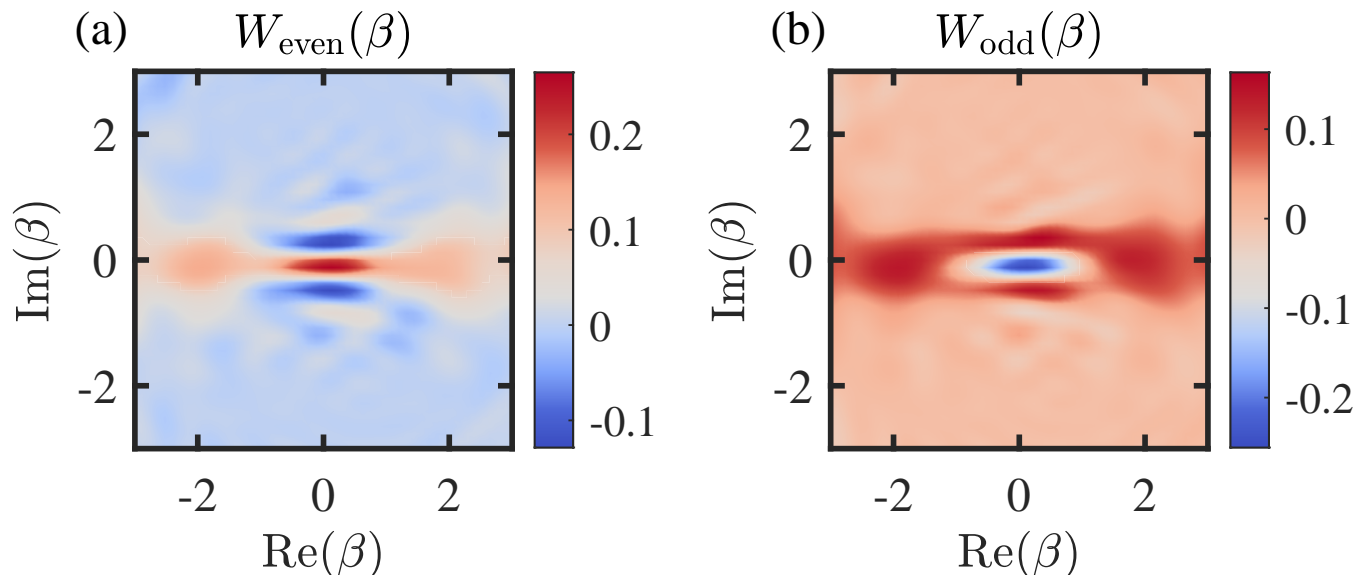


FIG. S15: Numerical Wigner tomography for final state after the Dicke-model SPT, governed by the full Hamiltonian. (a) Wigner functions associated with the collective even-parities of the qubits. (b) Wigner functions associated with the collective odd-parities of the qubits.

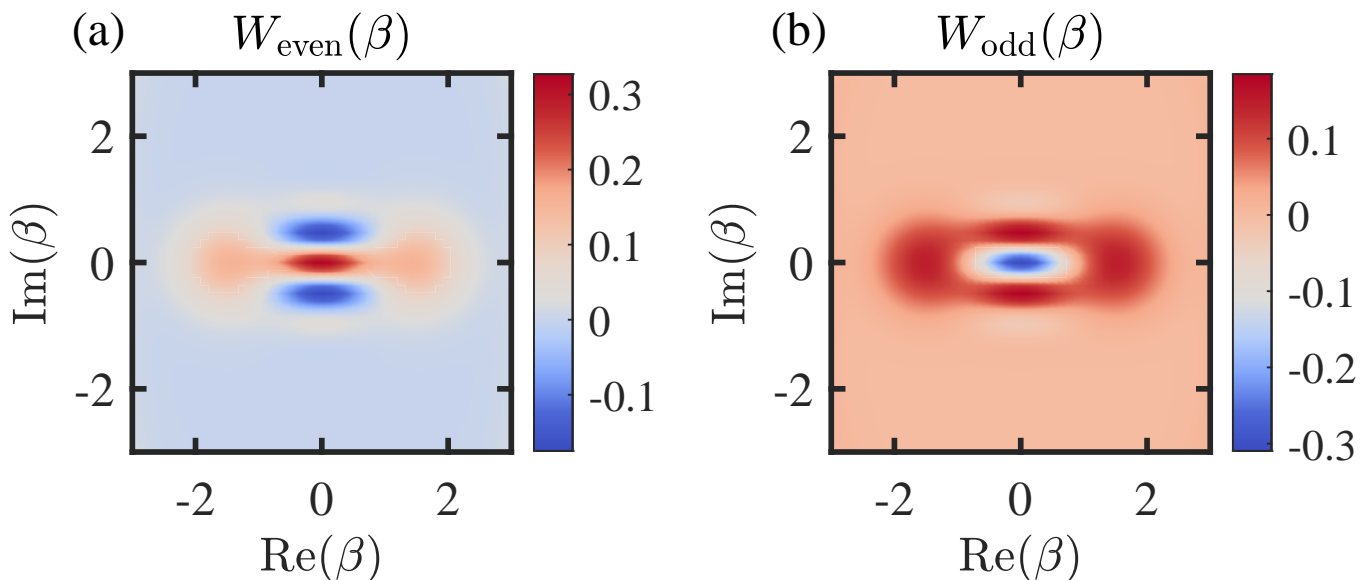


FIG. S16: Numerical Wigner tomography for final state after the Dicke-model SPT, deduced by the ground state of the Dicke-model Hamiltonian. (a) Wigner functions associated with the collective even-parities of the qubits. (b) Wigner functions associated with the collective odd-parities of the qubits.

$\nu_2 = 2KJ_0(\mu)$ with $\mu = \varepsilon_1/\nu_1$, the system dynamics in the interaction picture can be effectively described by the Dicke Hamiltonian with $\eta = \sqrt{N}\lambda J_2(\mu)/2$ and $\Omega = \varepsilon_2/2$.

To confirm the validity of the approximations for deriving the effective Hamiltonian, we perform numerical simulations for the 10-qubit Dicke model, in the symmetric Dicke subspace, without considering decoherence. We here set $\omega_p/(2\pi) = 5.581$ GHz, $\lambda/(2\pi) = 19.91$ MHz, $K/(2\pi) = 19.91$ MHz, $\varepsilon_1/(2\pi) = 207.31$ MHz, $\nu_1/(2\pi) = 250$ MHz, and $\nu_2/(2\pi) = 33.28$ MHz. With this setting, ξ can be controlled by ω_0 and ε_2 . With this setting, ξ can be controlled by ω_0 and ε_2 . The average photon number, simulated for the quenching process where δ and ε_2 are varied as $\delta = \varepsilon_2 = 2\eta/\xi(t)$, with $\xi(t) = 0.6 + 0.9t/t_f$ (t_f the total quench time), is shown in Fig. S14(a), which well agrees with

the result obtained from the even ground state of the ideal Hamiltonian (Fig. S14(b)). The quenching process starts with the state $|0\rangle \prod_{j=1}^N |g_j\rangle$. The Wigner functions of the field, associated with the collective even- and odd-parities of the qubits after a quenching time $t = 2 \mu\text{s}$, are respectively displayed in Figs. S15(a) and S15(b). These field states are in well agreement with those based on the ideal ground states with the same parameter ξ , displayed in Figs. S16(a) and S16(b), respectively. These results imply that the presently demonstrated techniques can be used to realize the Dicke model and the associated SPT.

-
- [S1] M.-J. Hwang, R. Puebla, M. B. Plenio, “Quantum phase transition and universal dynamics in the Rabi model,” *Phys. Rev. Lett.* **115**, 180404 (2015).
- [S2] C. Song *et al.*, “Continuous-variable geometric phase and its manipulation for quantum computation in a superconducting circuit,” *Nat. Commun.* **8**, 1061 (2017).
- [S3] W. Ning *et al.*, “Deterministic entanglement swapping in a superconducting circuit,” *Phys. Rev. Lett.* **123**, 060502 (2019).
- [S4] C. Song *et al.*, “10-qubit entanglement and parallel logic operations with a superconducting circuit,” *Phys. Rev. Lett.* **119**, 180511 (2017).
- [S5] Q.-X. Mei *et al.*, “Experimental realization of the Rabi-Hubbard model with trapped ions,” *Phys. Rev. Lett.* **128**, 160504 (2022).
- [S6] M. Hofheinz *et al.*, “Synthesizing arbitrary quantum states in a superconducting resonator,” *Nature* **459**, 546–549 (2009).
- [S7] D. M. Meekhof, *et al.*, “Generation of nonclassical motional states of a trapped atom,” *Phys. Rev. Lett.* **76**, 1796–1799 (1996).
- [S8] D. Leibfried, *et al.*, “Quantum dynamics of single trapped ions,” *Rev. Mod. Phys.* **75**, 281–324 (2003).
- [S9] D. Lv *et al.*, “Quantum simulation of the quantum Rabi model in a trapped ion,” *Phys. Rev. X* **8**, 021027 (2018).
- [S10] M.-L. Cai *et al.*, “Observation of a quantum phase transition in the quantum Rabi model with a single trapped ion,” *Nat. Commun.* **12**, 1126 (2021).
- [S11] M. Grant, S. Boyd, CVX: Matlab software for disciplined convex programming, version 2.0 beta. <http://cvxr.com/cvx>, September (2013).
- [S12] G. Vidal, R. F. Werner, “Computable measure of entanglement,” *Phys. Rev. A* **65**, 032314 (2002).
- [S13] W. P. Schleich, “Quantum Optics in Phase Space,” (Wiley-VCH, Berlin, 2001).
- [S14] N. K. Langford *et al.*, “Experimentally simulating the dynamics of quantum light and matter at deep-strong coupling,” *Nat. Commun.* **8**, 1715 (2017).
- [S15] M. Tavis, F. W. Cummings, “Exact solution for an N -molecule-radiation-field Hamiltonian,” *Phys. Rev.* **170**, 379 (1968).
- [S16] C. Song *et al.*, “Generation of multicomponent atomic Schrödinger cat states of up to 20 qubits,” *Science* **365**, 574 (2019).
- [S17] Clive Emary, Tobias Brandes, “Quantum chaos triggered by precursors of a quantum phase transition: The Dicke model,” *Phys. Rev. Lett.* **90**, 044101 (2003).
- [S18] Pierre Nataf, Cristiano Ciuti, “Protected quantum computation with multiple resonators in ultrastrong coupling circuit QED,” *Phys. Rev. Lett.* **107**, 190402 (2011).